Journal of
Materials Chemistry A

Accepted Manuscript

Journal of
Materials Chemistry A

Materials for energy and sustainability
www.rsc.org/MaterialsA

Volume 4 | Number 1 | 7 January 2016 | Pages 1–330

ISSN 2050-7488

ROYAL SOCIETY OF CHEMISTRY

PAPER
Kun Chang, Zhaorong Chang et al.
Bubble-template-assisted synthesis of hollow fullerene-like
MoS₂ nanocages as a lithium ion battery anode material

175 YEARS

This is an Accepted Manuscript, which has been through the Royal Society of Chemistry peer review process and has been accepted for publication.

Accepted Manuscripts are published online shortly after acceptance, before technical editing, formatting and proof reading. Using this free service, authors can make their results available to the community, in citable form, before we publish the edited article. We will replace this Accepted Manuscript with the edited and formatted Advance Article as soon as it is available.

You can find more information about Accepted Manuscripts in the author guidelines.

Please note that technical editing may introduce minor changes to the text and/or graphics, which may alter content. The journal's standard Terms & Conditions and the ethical guidelines, outlined in our author and reviewer resource centre, still apply. In no event shall the Royal Society of Chemistry be held responsible for any errors or omissions in this Accepted Manuscript or any consequences arising from the use of any information it contains.

ROYAL SOCIETY OF CHEMISTRY

rsc.li/materials-a

Cyanide-metal framework derived CoMoO$_4$/Co$_3$O$_4$ hollow porous octahedrons as advanced anode for high performance lithium ion batteries

*Yingying Chen,[a,b] Yue Wang,[b] Xiaoping Shen,[*a] Rong Cai,[b] Hongxun Yang,[b] Keqiang Xu,[a] Aihua Yuan [b] and Zhenyuan Ji [a]*

[a] School of Chemistry & Chemical Engineering, School of Material Science and Engineering, Jiangsu University, Zhenjiang 212013, PR China

[b]School of Environmental & Chemical Engineering, Jiangsu University of Science and Technology, Zhenjiang 212003, PR China

[*]Corresponding author: Xiaoping Shen,

Email address: xiaopingshen@163.com

Abstract: In this work, $CoMoO_4/Co_3O_4$ hollow porous octahedrons are synthesized by thermal conversion of a cyanide-metal framework (CMF) compound of $Co_2[Mo(CN)_8]\cdot xH_2O$. As anode materials for lithium ion batteries (LIBs), the $CoMoO_4/Co_3O_4$ electrodes exhibit a remarkably improved electrochemical performance in terms of large lithium storage capacity (1175.1 mA h g^{-1} at 200 mA g^{-1}), high initial coulombic efficiency (86.9%), outstanding cycling stability (96.9% capacity retention after 100 cycles) and remarkable rate capability (924.2 mA h g^{-1} at 2000 mA g^{-1}). The excellent electrochemical performance of the $CoMoO_4/Co_3O_4$ composite can be ascribed to the hollow porous structure and the possible synergistic effect of different components, which could provide more efficient charge storage sites, shorten ion diffusion and electron transport path, and accommodate the volume change during cycling. The facile synthesis strategy and excellent lithium storage performance render the $CoMoO_4/Co_3O_4$ hollow porous octahedrons a promising candidate for high-performance LIBs anode materials.

Keywords: Hollow porous octahedrons; Cyanide-metal framework; $CoMoO_4$; Co_3O_4; Lithium ion batteries

1. Introduction

Energy problem is always an important factor restricting the development of social economy.[1-4] Lithium ion batteries (LIBs) has become the most popular generation of storage battery due to its prominent characteristics of high specific energy, high voltage and long service life.[5-8] During the process of seeking high performance LIBs, transitional metal oxides such as Co_3O_4,[9-13] MoO_3,[14,15] Fe_2O_3,[16-18] Fe_3O_4,[19-21] MnO_2,[22] SnO_2,[23-25] etc. are considered to be the promising anode materials because of their excellent physical and chemical properties as well as superior theoretical capacities compared to 372 mA h g^{-1} of graphite. However, large initial irreversible capacities and poor cycling stability resulting from volume changes during the lithiation and delithiation processes usually result in fast capacity fading and further greatly impede their practical application.[26,27] Although constructing nanostructured transition metal oxides with different morphologies is expected to be an effective strategy to improve their electrochemical performance, many single-metal oxides remain suffering from poor cycling stability.[28-32] Alternatively, ternary transition-metal oxides have attracted increasing research interest in recent years. The complex chemical compositions and the synergic effects of various metal elements in these materials lead to their remarkable electrochemical performance.[33] Recently, a ternary transitional oxide of $CoMoO_4$ has emerged as an attractive anode material due to its feasible oxidation state, high conductivity and high theoretical specific capacity (980 mA h g^{-1}).[34-37] During electrochemical reaction, $CoMoO_4$ quickly converts to Co_3O_4 and MoO_3 nanocomposites dispersed in Li_2O matrix, which offers a buffering effect for the volume change in the charge/discharge process.[38-41] Besides abundant oxidation states of Mo (from +III to +VI), the low potential of conversion reactions can also help to obtain much higher specific capacity and energy density. For example, Christie *et al.* reported $CoMoO_4$ submicrometer particles with a reversible capacity of 990 mA h g^{-1} at a current density of 100 mA g^{-1}.[42] Recent studies also demonstrated that $CoMoO_4/M_xO_y$ (M = Fe, Co) nanocomposites delivered better electrochemical properties than pure $CoMoO_4$. Yang *et al.* prepared $Co_3O_4/CoMoO_4$ hollow spheres

through one-pot solvothermal method followed by a thermal treatment process, and the $Co_3O_4/CoMoO_4$ heterostructures exhibited much better electrocatalytic activity for the oxygen evolution reaction than $CoMoO_4$.[43] Wang *et al.* synthesized $CoMoO_4/Fe_2O_3$ core-shell nanorods by a two-step hydrothermal method, and the core-shell nanorods as LIBs anode exhibited a high reversible capacity of 1354 mA h g^{-1} at 0.2 C rate, which is higher than that of bare $CoMoO_4$ nanorods.[44] In addition, designing electrode materials with hollow porous structures could also enhance the electrochemical properties of $CoMoO_4$ as LIBs anodes.[45, 46] Despite some progresses, to develop simple and effective methods for the fabrication of hollow porous Mo-based mixed oxides with satisfactory performances still remains a big challenge.

Recently, cyanide-metal framework (CMF) compounds, a class of designable porous materials with metal ions bridged by cyano-groups, have been demonstrated to be ideal precursors for preparing various hollow/porous metal oxide materials. This method firstly synthesizes CMF micro/nanoparticles with specific morphologies, and then calcinates the CMF precursors in a proper temperature to obtain hollow/porous metal oxides with a good morphological maintenance. To date, a variety of metal oxide materials such as Fe_2O_3 porous microboxes,[47] Co_3O_4 porous nanocages,[48] SnO_2-Fe_2O_3 nanocubes,[49] Fe_2O_3-CuO porous cubes,[50] ZnO/Co_3O_4 nanocomposite clusters,[51] Fe_2O_3-NiO microflowers,[52] $Mn_xCo_{3-x}O_4$ porous nanocubes,[53] $CoFe_2O_4$ hollow porous nanocubes,[54] $Fe_2O_3@NiCo_2O_4$ nanocages,[55] $FeCo_2O_4$ hollow nanospheres,[56] AFe_2O_4 (A=Ni, Zn, Co) hollow boxes,[57] $Mn_{1.8}Fe_{1.2}O_4$ porous nanocubes [58] have been successfully prepared by the CMF precursor method, and they all show remarkably enhanced electrochemical performances for LIBs anodes. Thus, the CMF precursor route provides a unique opportunity to develop highly tailorable new LIBs anode materials. However, to the best of our knowledge, present study on CMF-based metal oxides mainly focus on hexacyanometallates-based CMF precursors (Prussian blue and its analogues), in which the metal elements are mainly limited to the first row transition metals such as Fe, Co, Ni, Zn, Cu and Mn, while the second and third transition elements can rarely be achieved. In contrast, octacyanometallates-based CMFs can supply the second and third transition elements,

especially Mo and W. In this regard, the development of Mo-based oxides based on octacyanometallates-based precursors would be a facile and effective route. However, hollow/porous Mo-based oxides derived from octacyanometallates-based precursors have not been reported until now.

Herein, $CoMoO_4/Co_3O_4$ hollow porous octahedrons were successfully synthesized by using a octacyanometallates-based CMF precursor of $Co_2[Mo(CN)_8] \cdot xH_2O$. Benefiting from the hollow porous structure and the synergistic effect of the different components, the as-prepared $CoMoO_4/Co_3O_4$ electrode exhibits excellent lithium-storage performance. This study further demonstrates that the CMF precursor strategy is a facile and highly effective approach to synthesize a wide range of hollow porous metal oxides for energy storage applications.

2. Experimental section

Chemicals. Poly(vinyl pyrrolidone) (PVP, K-30; average M_w = 40000), $CoCl_2 \cdot 6H_2O$, acetone and absolute ethanol were of analytical grade and purchased from Shanghai Chemical Reagent Co., Ltd (China). All of them were used without further purification. Double distilled water was used in all the experiments. $K_4[Mo(CN)_8] \cdot 2H_2O$ was prepared according to literature procedures.[59, 60]

Synthesis of $CoMoO_4/Co_3O_4$ hollow porous octahedrons. In a typical procedure, 0.043 g (0.18 mmol) of $CoCl_2 \cdot 6H_2O$ and 2 g of PVP (K-30) were dissolved in 60 mL water to form a clear solution A. Meanwhile, 0.045 g (0.09 mmol) of $K_4[Mo(CN)_8] \cdot 2H_2O$ was dissolved in 30 mL water to form another clear solution B. Then, solution B was slowly added into A under magnetic stirring. After stirring at 30 °C for 1 h, an orange suspension solution was obtained. 30 mL of acetone were then added to precipitate the precursor $Co_2[Mo(CN)_8] \cdot xH_2O$. Subsequently, the precursor product was collected by centrifugation, washed several times with absolute ethanol then dried in air. To get the final $CoMoO_4/Co_3O_4$ hollow porous octahedrons, the as-obtained precursor were annealed at 450 °C for 2 h in air with a heating rate of 2 °C min^{-1}.

Material characterization

The structure, morphology and size of obtained products were characterized by X-ray diffraction (XRD) (Shimadzu XRD-6000 diffractometer) using Cu-K_α radiation (λ= 1.5406 Å), field emission scanning electron microscopy (FE-SEM, ZEISS Merlin Compact) and transmission electron microscopy (TEM, JEM-2100). The compositions of the products were analyzed by energy-dispersive X-ray spectrometry (EDX) attached to the FESEM and X-ray photoelectron spectroscopy (XPS, Thermo ESCALAB 250). Raman scattering was performed on a DXR Raman spectrometer using a 532 nm laser source. The specific surface areas and pore size distributions were measured by Micromeritics ASAP2020 using N_2 adsorption-desorption isotherms at liquid nitrogen temperature of 77 K. Thermo-gravimetric (TG) analysis was performed using a Perkin-Elmer Diamond TG/DTA instrument at a heating rate of 10 °C min^{-1} in air.

Electrochemical measurements

The Li-storage performances of the sample were tested on a LANDCT2001A test system using CR2032 coin-type half cells. The working electrodes were prepared by mixing 70 wt% of $CoMoO_4$/Co_3O_4, 20 wt% of Super P and 10 wt% of sodium carboxymethyl cellulose (CMC) in water. The resulting slurry was pasted onto copper foil，then dried in a vacuum oven at 80 °C overnight. Lithium foil and microporous polypropylene film were used as the counter electrode and separator, respectively. 1 M of $LiPF_6$ in ethylene carbonate/diethyl carbonate (1:1 v/v) was used as electrolyte. The active mass loading on the electrode was about 0.89 mg cm^{-2}. The cell assembly was carried out in an Ar-filled glovebox with moisture and oxygen concentrations below 1ppm. The charge/discharge characteristics were determined through cycling in the potential range of 0.01-3 V at diverse current densities. Cyclic voltammetry (CV) measurements were performed on an electrochemical workstation (Autolab PGSTAT302N) between 3.0 and 0.01 *vs* (Li/Li$^+$)/V at a sweep rate of 0.2 mV s^{-1}. Electrochemical impedance spectroscopy (EIS) tests were recorded from 100 kHz to 0.01Hz with *ac* amplitude of 10 mV.

3. Results and discussion

The strategy to synthesize $CoMoO_4/Co_3O_4$ hollow porous octahedrons is depicted in Fig. 1. $Co_2[Mo(CN)_8]\cdot xH_2O$ octahedral micro-crystals were firstly prepared by the reaction of Co^{2+} and $[Mo(CN)_8]^{4+}$ with the assistance of PVP. $CoMoO_4/Co_3O_4$ hollow porous octahedrons were then achieved by thermal decomposition of $Co_2[Mo(CN)_8]\cdot xH_2O$ precursor at 450 °C for 2 h. The phase structure of as-prepared $Co_2[Mo(CN)_8]\cdot xH_2O$ micro-crystal precursor is inspected by XRD in Fig. 2a. All the diffraction peaks can be assigned to the tetragonal system of $Co_2[Mo(CN)_8]\cdot xH_2O$.[61] Thermogravimetric analysis of $Co_2[Mo(CN)_8]\cdot xH_2O$ indicates two main weight-loss processes (Fig. 2b). The first weight loss of 24.70 wt% from room temperature to 190 °C can be ascribed to the loss of crystal water and adsorbed water molecules in the porous framework structure. The second weight loss of 23.94 wt% from 190 °C to 400 °C can be attributed to the breakdown of the cyanide-metal framework. Above 400 °C, no weight loss is observed until 800 °C. Based on the above TG results, 450 °C is chosen as the annealing temperature for the formation of $CoMoO_4/Co_3O_4$ hollow porous structure.
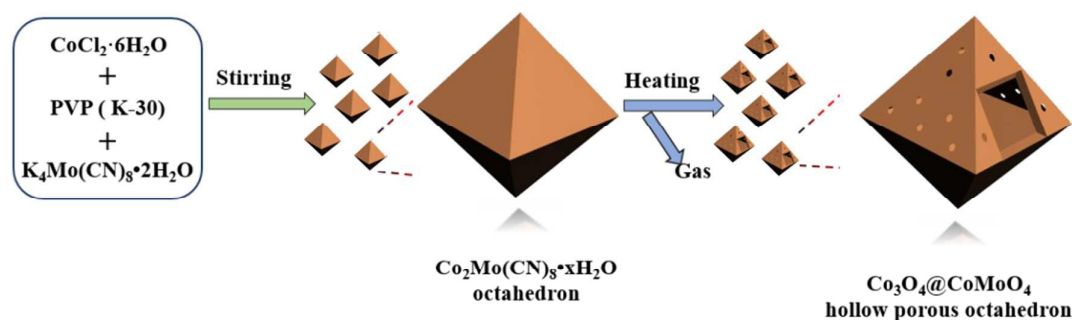
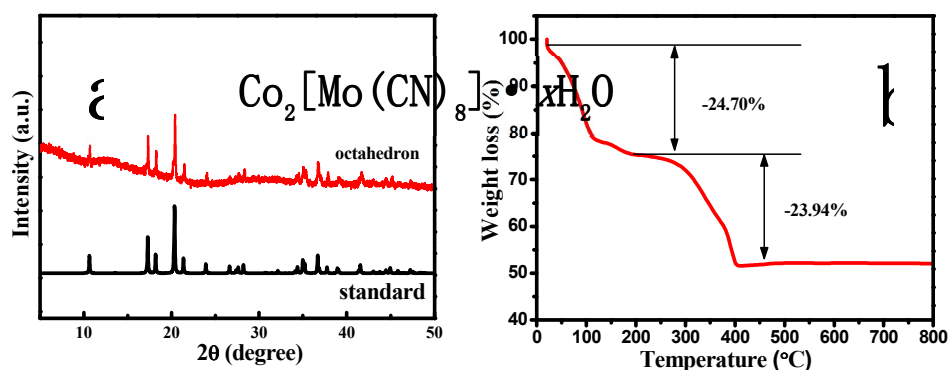**Fig.1** Schematic illustration of the formation process of $CoMoO_4/Co_3O_4$ hollow porous octahedrons.

Fig. 2 (a) XRD pattern and (b) TG curve of the as-prepared $Co_2[Mo(CN)_8]\cdot xH_2O$ precursor.

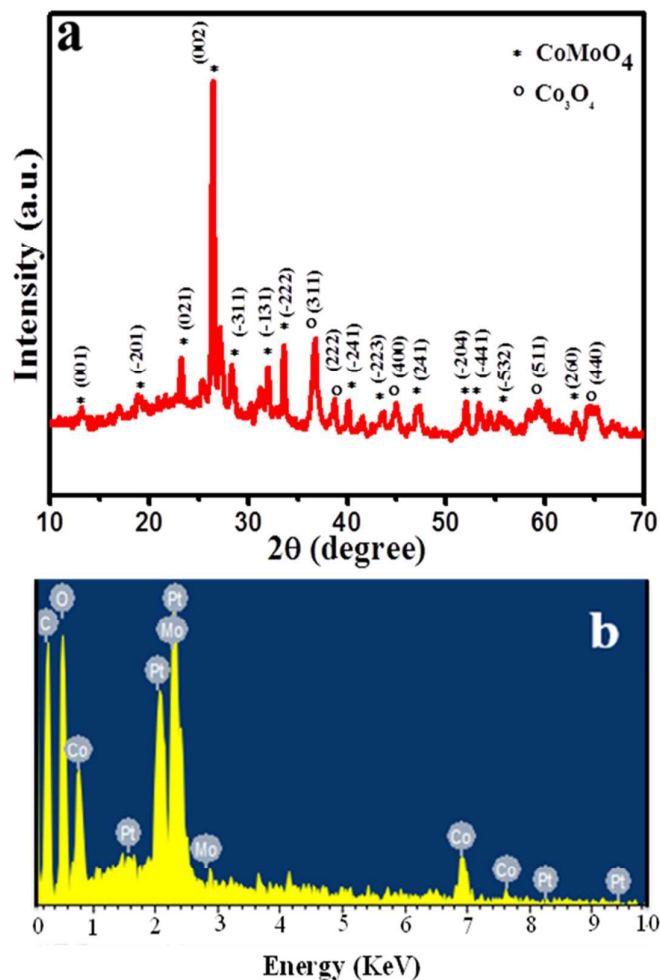**Fig. 3** (a) XRD pattern and (b) EDS spectrum of $CoMoO_4/Co_3O_4$ hollow porous octahedrons.

The typical XRD pattern of final calcination product is shown in Fig. 3a. All the diffraction peaks can be indexed to monoclinic $CoMoO_4$ (JCPDS No: 21-0868) and

Journal of Materials Chemistry A

tetragonal Co_3O_4 (JCPDS No: 43-1003). This result confirms that the annealing product is a composite of $CoMoO_4$ and Co_3O_4. Furthermore, energy dispersive spectroscopy (EDS) of $CoMoO_4/Co_3O_4$ (Fig. 3b) reveals that the molar ratio of Co to Mo is about 2:1 (Table S1), which is well consistent with the composition of the $Co_2[Mo(CN)_8]\cdot xH_2O$ precursor. The Pt and C peaks in the EDS spectrum come from the Pt film and the carbon substrate in the SEM measurement.
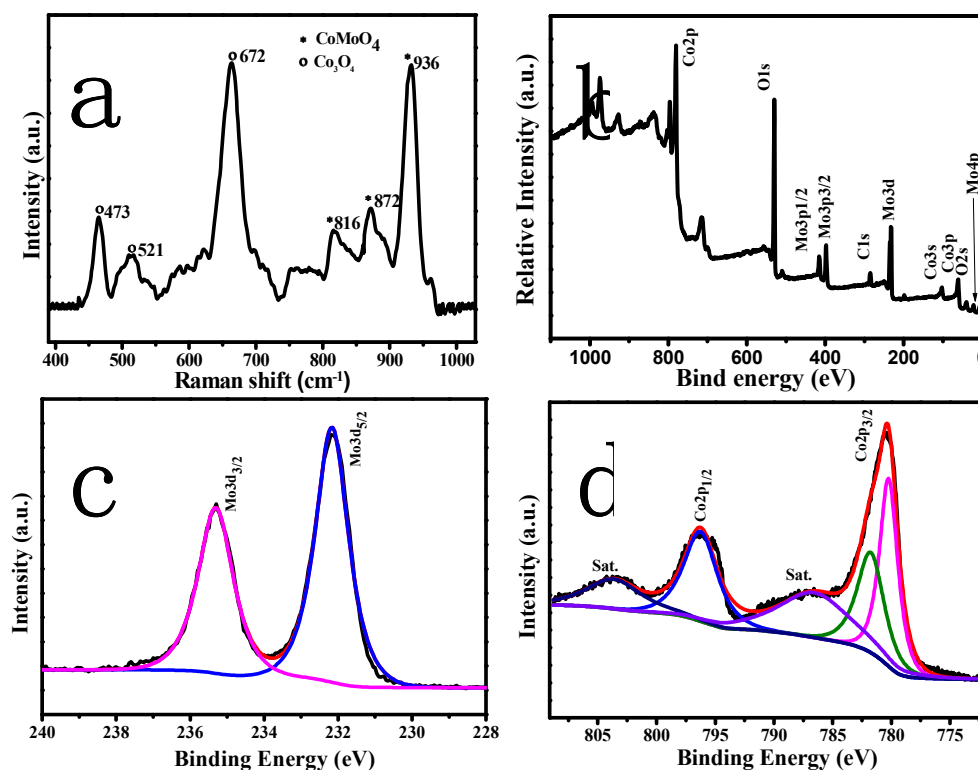
Fig. 4 (a) Raman spectra of $CoMoO_4/Co_3O_4$. (b) XPS survey scan of $CoMoO_4/Co_3O_4$. High-resolution XPS spectra of (c) Mo 3d and (d) Co 2p.

The structural and constitution information of the as-obtained porous $CoMoO_4/Co_3O_4$ products were further studied by Raman spectroscopy and X-ray photoelectron spectroscopy (Fig. 4). As shown in Fig. 4a, the peaks at 473, 521, and 672 cm^{-1} correspond to E_g, F_{2g}, and A_{1g} models of Co_3O_4, respectively.[62] The other bands at 816, 872 and 936 cm^{-1} can be ascribed to $CoMoO_4$.[63] Fig. 4b displays the full-survey-scan XPS spectrum of the $CoMoO_4/Co_3O_4$, which indicates the presence

of Co, Mo, O and C elements. As shown in Fig. 4c, the splitting doublet of Mo $3d_{3/2}$ and Mo $3d_{5/2}$ at 232.1 and 235.3 eV with the region width ΔMo 3d = 3.2 eV is characteristics of the Mo (VI) oxidation state in $CoMoO_4$.[43] The Co2p XPS spectrum (Fig. 4d) presents two major peaks centered at 796.3 and 780.4 eV, which can be attributed to $Co2p_{1/2}$ and $Co2p_{3/2}$, respectively. The $Co2p_{3/2}$ peaks can be further deconvoluted into two peaks at 780.3 and 781.9 eV, corresponding to Co(II) and Co(III), respectively,[43,64] which is consistent with the composition of $CoMoO_4/Co_3O_4$. The O1s spectrum (Fig. S1) exhibits one peak at 529.9 eV, corresponding to the lattice oxygen.[45] Therefore, the Raman and XPS results further prove that the as-synthesized product is $CoMoO_4/Co_3O_4$.
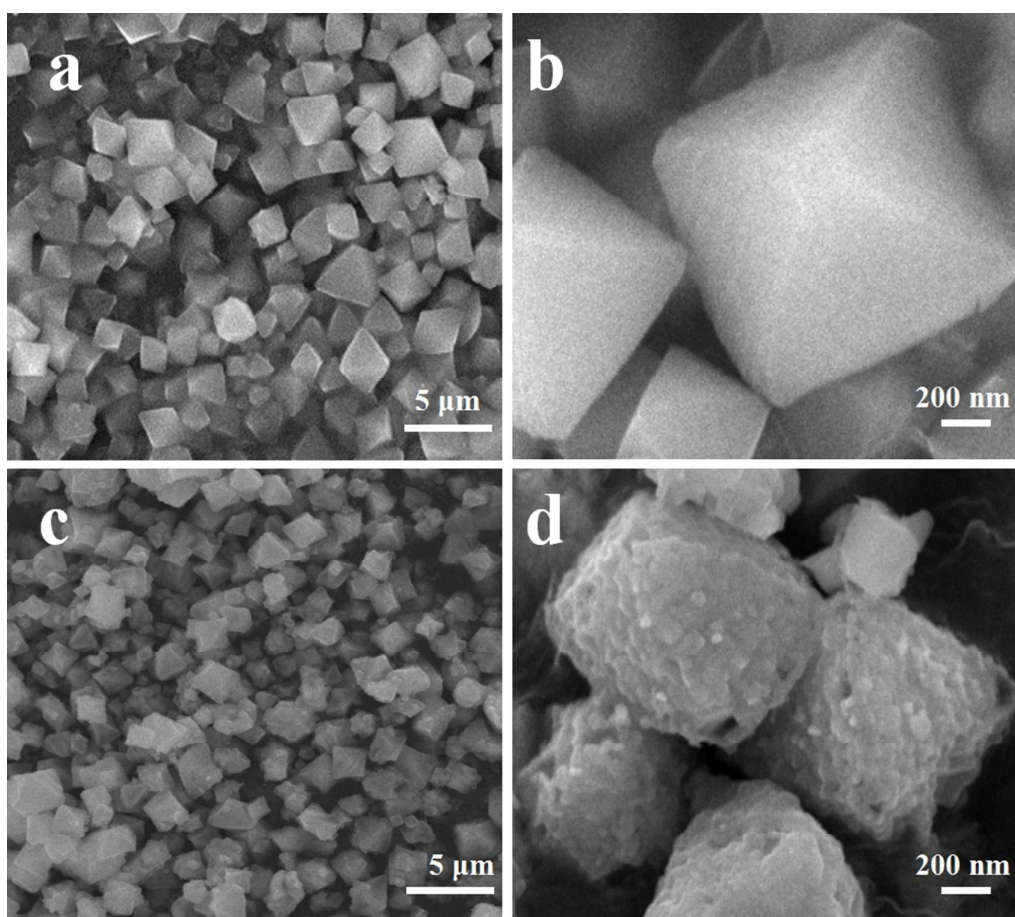
Fig. 5 FESEM images of (a, b) $Co_2[Mo(CN)_8] \cdot xH_2O$ octahedrons and (c, d) $CoMoO_4/Co_3O_4$ hollow porous octahedrons.

The morphologies and sizes of the as-prepared samples were inspected by field-emission scanning electron microscopy (FESEM) (Fig. 5). As can be seen from

Fig. 5a and 5b, $Co_2[Mo(CN)_8] \cdot xH_2O$ exhibits well-defined octahedral morphology with a smooth surface and an average side-length of *ca*. 1.2 μm. FESEM images (Fig. 5c and 5d) of $CoMoO_4/Co_3O_4$ reveal that the octahedron-shaped morphology is maintained after the calcination, while the size is reduced to *ca*. 1 μm in side-length with a rather rough surface due to the decomposition of CN^- to CO_2 and N_xO_y gases. It can be clearly seen from Fig. 5d that the rough surface is composed of numerous interconnected nanoparticles (50-60 nm in diameter). TEM was conducted to clarify the interior structures of these octahedrons. As shown in Fig. 6a and 6b, most of the $CoMoO_4/Co_3O_4$ octahedrons exhibit well-defined hollow structures with loaded nanoparticles (Fig. 6a, inset). For a few particles, the hollow structures cannot be clearly observed, which is probably because the electron beam cannot penetrate them completely due to their big size or thick shell. The high-resolution TEM (HRTEM) image (Fig. 6c) shows clear lattice fringes with spacings of 0.336 and 0.243 nm, which correspond to the (002) plane of $CoMoO_4$ and the (311) plane of Co_3O_4, respectively.

Journal of Materials Chemistry A Accepted Manuscript
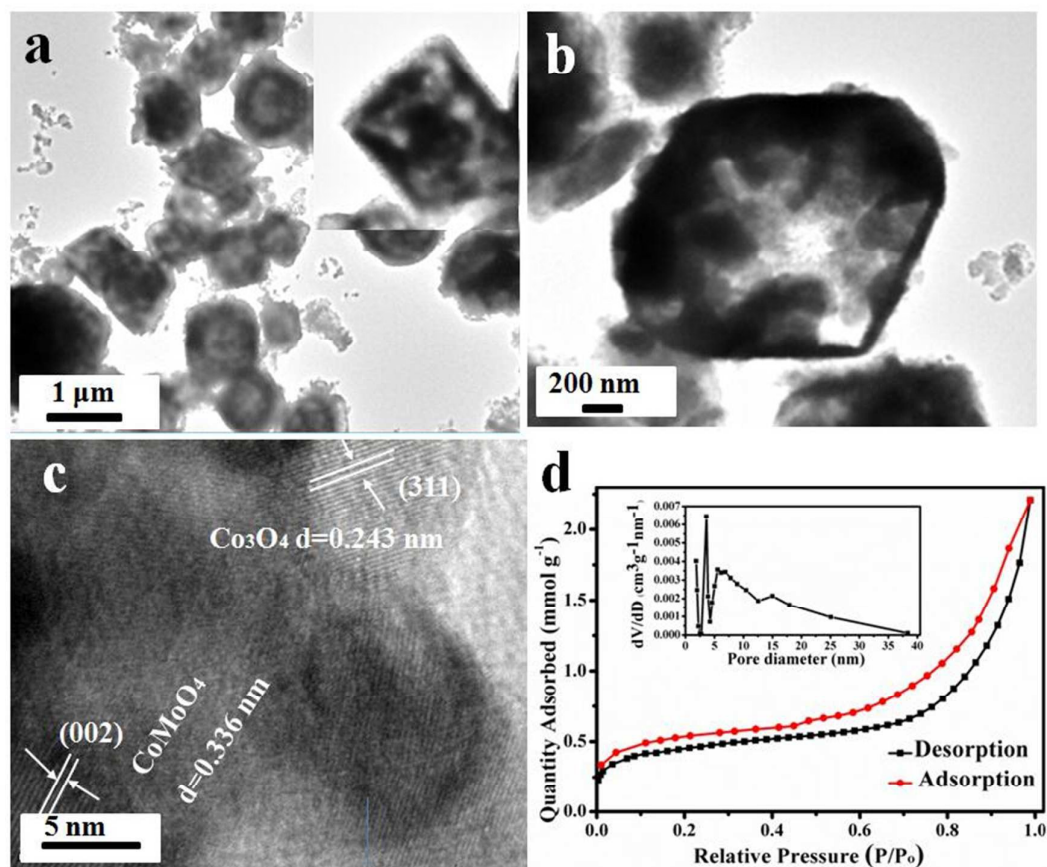
Fig. 6 (a, b) TEM and (c) HRTEM images of $CoMoO_4/Co_3O_4$. (d) N_2 adsorption/desorption isotherms (77 K) and pore size distributions (inset) of $CoMoO_4/Co_3O_4$.

The nitrogen adsorption-desorption isotherms are measured to obtain the specific surface area and pore size distribution of $CoMoO_4/Co_3O_4$. As shown in Fig. 6d, the material shows a type-IV isotherm with a distinct hysteresis loop, indicating the presence of mesoporous structure. The $CoMoO_4/Co_3O_4$ hollow porous octahedrons have a much higher specific surface (33.81 $m^2\,g^{-1}$) than that of $Co_2[Mo(CN)_8]\cdot xH_2O$ precursor (10.57 $m^2\,g^{-1}$, Fig. S2). The typical pore size distribution (Fig. 6d, inset) calculated from BJH method shows a multiple distribution with a wide pore-size distribution between 2 and 25 nm and a narrow distribution centered at 1.8 nm, which indicates the micro/mesopore porous shell. Such a micro/mesopore structure could effectively provide more charge storage sites, shorten ion/electron diffusion distance and accommodate the stress relaxation during the repeated Li^+ charge-discharge

process.
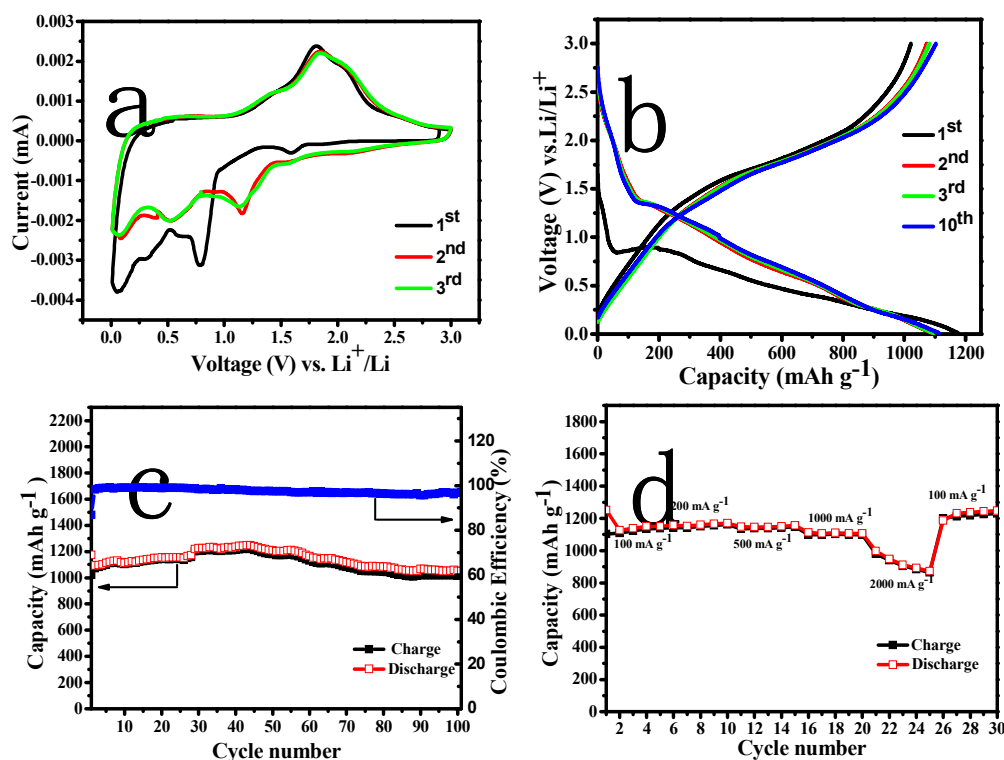
Fig. 7 Electrochemical performances of $CoMoO_4/Co_3O_4$ hollow porous octahedrons as anode materials for LIBs: (a) representative CVs in the voltage range of 0.01-3.0 V vs. Li/Li^+ at a scan rate of 0.2 mV s^{-1}. (b) discharge-charge voltage profiles at a current density of 200 mA g^{-1}. (c) cycling performance over 100 cycles at 200 mA g^{-1}. (d) rate capability at different current densities.

The electrochemical performances of $CoMoO_4/Co_3O_4$ hollow porous octahedrons as anode for LIBs were investigated by a standard half-cell testing system. As expected, $CoMoO_4/Co_3O_4$ electrode exhibits excellent electrochemical performance. Fig. 7a shows the CV curves of $CoMoO_4/Co_3O_4$ in the first three cycles at a scan rate of 0.2 mV s^{-1} in the potential range of 0.01-3 V *vs*. Li/Li^+. In the first cathodic scan, two reduction peaks around 1.6 and 0.8 V can be assigned to the reduction of Co_3O_4 and $CoMoO_4$ to metallic Co and Mo.[38,43] Another cathodic peak at 0.3 V was usually related to the formation of irreversible solid electrolyte interphase (SEI) layer, which

disappeared during the following cycles.[65-67] During the anodic scan, two major oxidation peaks at 1.5 and 1.8 V can be related to the oxidation of Co^0 and Mo^0.[68-70] After the first cycle, the main cathodic peak appeared at around 1.1 and 0.5 V, indicating the different reduction mechanisms from the first one, which might be attributed to the sequential insertion of Li^+ ions into to CoO and MoO_3.[34,35,42] Good reproducibility of CV curves from the 2nd cycle manifests good reversibility of the $CoMoO_4/Co_3O_4$ electrode. Based on the CV measurements and the storage mechanisms of Co_3O_4 and $CoMoO_4$, the probable electrochemical reactions are listed as follows:
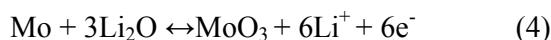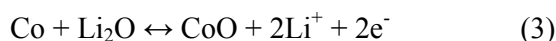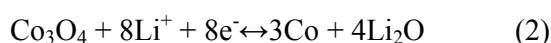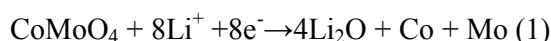
$$CoMoO_4 + 8Li^+ + 8e^- \rightarrow 4Li_2O + Co + Mo \quad (1)$$

$$Co_3O_4 + 8Li^+ + 8e^- \leftrightarrow 3Co + 4Li_2O \quad (2)$$

$$Co + Li_2O \leftrightarrow CoO + 2Li^+ + 2e^- \quad (3)$$

$$Mo + 3Li_2O \leftrightarrow MoO_3 + 6Li^+ + 6e^- \quad (4)$$

Fig. 7b exhibits the 1st, 2nd, 3rd and 10th discharge-charge curves of $CoMoO_4/Co_3O_4$ electrode at a constant current density of 200 mA g^{-1}. There is an apparent plateau at around 0.8 V in the first discharge curve, indicating the reduction of Mo^{6+}, which is well consistent with the CV results. From the second discharge curve, the voltage flat plateau is substituted by a short plateau (~1.45 V) due to a heterogeneous reaction mechanism between Li^+ and the electrode materials.[44,45] The initial discharge and charge capacities are 1175.1 and 1021.3 mA h g^{-1}, respectively. It is worth noting that $CoMoO_4/Co_3O_4$ electrode shows relatively low irreversible capacity loss in the initial cycle with the coulombic efficiency of 86.9%. The capacity loss in the first cycle is attributed to the SEI formation. The 2nd, 3rd and 10th discharge/charge capacities of the $CoMoO_4/Co_3O_4$ electrode are 1092.5/1073.2, 1096.1/1081.6 and 1112.7/1103.2 mA h g^{-1}, respectively, indicating a high capacity performance and excellent capacity retention.

The long cycle life and high rate capability are both important targets for LIBs in practical applications. Fig. 7c shows the cycling performance of the $CoMoO_4/Co_3O_4$ electrode at 200 mA g^{-1}. The capacity shows a gradual increase after the second cycle

and then declines after about 50 cycles. At the 100th cycle, the $CoMoO_4/Co_3O_4$ electrode still maintains a reversible capacity of 1050.3 mA h g^{-1} with good capacity retention of 96.1%, which is higher than previously reported $CoMoO_4$-based electrodes (Table S2), indicative of the advantages of the $CoMoO_4/Co_3O_4$ composite over single $CoMoO_4$ anodes. The coulombic efficiency shows a slight decrease after around 50 cycles, which may be related with the decreasing capacity after 50 cycles, suggesting a possible decay in charge-discharge reversibility. Rate performance of $CoMoO_4/Co_3O_4$ electrode was also explored at different current densities. As shown in Fig. 7d, the electrode exhibits great rate performance with average discharge capacities of 1163.5，1161.7, 1149.9 and 1108.8 mAh g^{-1} at current densities of 100, 200, 500 and 1000 mA g^{-1}, respectively. Even at a high current density of 2000 mA g^{-1}, the discharge capacity is still retained at 924.2 mA h g^{-1}. What's more, the discharge capacity quickly recovers to around 1200 mA h g^{-1} once the current density returns to 100 mA g^{-1}. Such an outstanding rate performance would endow $CoMoO_4/Co_3O_4$ promising application in high-power LIBs. It is interesting to note that the capacities at the current density of 200 mA g^{-1} are almost no reduction compared to those at 100 mA g^{-1}, which could result from the gradual increase in capacity during cycling at 100 mA g^{-1} due to the activation of the porous hollow structure (Fig. S3). It should be noted that the theoretical capacities of $CoMoO_4$ and Co_3O_4 are 980 mA h g^{-1} and 890 mA h g^{-1}, respectively.[10,34] Compared to the theoretical values of $CoMoO_4$ and Co_3O_4, the $CoMoO_4/Co_3O_4$ hollow porous octahedrons in our work exhibit higher reversible capacity of 1050.3 mA h g^{-1} at 200 mA g^{-1} after 100 cycles. The lithium storage performance of $CoMoO_4/Co_3O_4$ is also superior to some previously reported pure Co_3O_4 and MoO_3 (Table S3), demonstrating the advantages of ternary oxides over binary oxides as anode materials. The excellent lithium storage performance of $CoMoO_4/Co_3O_4$ can be ascribed to the unique hollow porous structure and the synergistic effect between $CoMoO_4$ and Co_3O_4 components. Firstly, the hollow porous structure can not only shorten ionic diffusion pathway and increase the contact area with electrolyte, but also accommodate the strain for volume expansion during cycles.[31,32] Secondly, during cycles, two components can achieve

better performance through a reinforcement or modification each other.[33] When $CoMoO_4$ or Mo react with Li^+, the Co_3O_4 or Co can serve as "buffer" to mitigate the stress and accommodate the large volume expansion. Thirdly, metallic Co and Mo nanoclusters can effectively enhance the electrical conductivity of the porous composite, resulting in an excellent rate performance.[43]
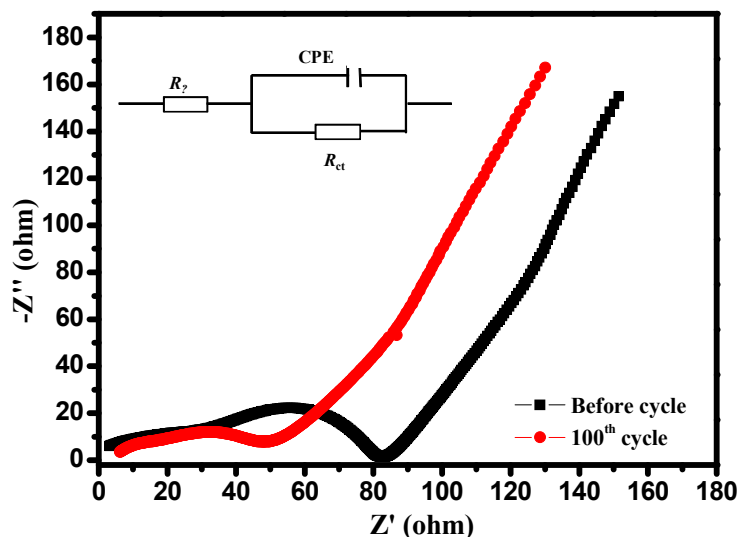
Fig. 8 Electrochemical impedance spectroscopy of the $CoMoO_4/Co_3O_4$ electrode before and after 100 cycles.

To further understand the fundamental electrochemical behavior of the electrode, EIS analyses of $CoMoO_4/Co_3O_4$ electrode before and after 100 cycles were measured and the corresponding Nyquist plots are shown in Fig. 8. Both plots show a quasi-semicircle at high frequency region and a sloping line in the low frequency region. The intercept at the Z-real axis at high frequency corresponds to the ohmic resistance (R_Ω), which represents the total resistance of the electrolyte, separator, and electrical contacts. The semicircle in the middle frequency range indicates the charge transfer resistance (R_{ct}) of the $CoMoO_4/Co_3O_4$ electrode/electrolyte interfacial region, and the inclined line in the low-frequency range represents the Warburg impedance, which represents the electrolyte diffusion in the porous electrode and proton diffusion in host materials.[71-73] The smaller the diameter of the semicircle is, the lower the

charge transfer resistance and better electrochemical dynamic action. It is clearly seen that $CoMoO_4/Co_3O_4$ electrode shows a smaller charge transfer resistance at the 100th cycle than the initial cycle, which are 50.2 and 81.3 Ω, respectively, based on the equivalent circuit (Fig. 8, inset), indicating improved electrical conductivity after cycles. This result further confirms the structure stabilizing role in the electrode. In conclusion, the $CoMoO_4/Co_3O_4$ material as anode for LIBs exhibits excellent lithium storage capacities, cycling stability and rate capability.

4. Conclusions

In summary, $CoMoO_4/Co_3O_4$ hollow porous octahedrons have been successfully synthesized through a facile thermolysis of CMF precursor. The as-synthesized $CoMoO_4/Co_3O_4$ exhibits a large lithium storage capacity of 1175.1 mA h g^{-1} at 200 mA g^{-1}, high initial coulombic efficiency of 86.9%, outstanding capacity retention of 96.9% after 100 cycles, and remarkable rate capability of 924.2 mA h g^{-1} at 2000 mA g^{-1}. The excellent electrochemical performance of the $CoMoO_4/Co_3O_4$ composite can be ascribed to its hollow porous nanostructures and the possible synergistic effect between $CoMoO_4$ and Co_3O_4 in the composite. This study demonstrates that the hollow porous $CoMoO_4/Co_3O_4$ is a promising anode material for LIBs, and the octacyanometallates-based CMF compounds are a promising class of precursors for the fabrication of novel hollow porous metal oxides with diversiform morphologies and fascinating compositions for electrochemical energy storage and other applications.

Acknowledgments

Notes and references

1 Z. Yang, J. Zhang, M. C. W. Kintner-Meyer, X. Lu, D. Choi, J. P. Lemmon and J. Liu, *Chem. Rev.*, 2011, 111, 3577–3613.

2 H. L. Wang, Q. L. Zhu, R. Q. Zou, and Q. Xu, *Chem 2*, 2017, 52–80.

3 H. B. Zhang, J. N. Nai, L. Yu and X. W. Lou, *Joule 1*, 2017, 77–107.

4 L.T. Yu, J. Liu, X.J. Xu, L.G. Zhang, R.Z. Hu, J.W. Liu, L.Z. Ouyang, L.C. Yang and M. Zhu, *ACS Nano.*, 2017, **11**, 5120–5129.

5 D. Larcher and J. M. Tarascon, *Nat. Chem.*, 2015, **7**, 19–29.

6 X. L. Dong, L. Chen, J. Y. Liu, S. Haller, Y. G. Wang and Y. Y. Xia, *Sci. Adv.*, 2016, **2**, e1501038.

7 X. J. Xu, J. Liu, Z.B. Liu, J. D. Shen, R. Z. Hu, J. W. Liu, L. Z. Ouyang, L. Zhang and M. Zhu, *ACS Nano.*, 2017, **11**, 9033–9040.

8 C. Xiao, and Y. Xie, *Joule 1*, 2017, 15-28.

9 N. Yan, L. Hu, Y. Li, Y. Wang, H. Zhong, X.Y. Hu, X. K. Kong and Q.W. Chen, *J. Phys. Chem. C*, 2012, **116**, 7227–7235.

10 J. Y. Wang, N. L. Yang, H. J. Tang, Z. H. Dong, Q. Jin, M. Yang, D. Kisailus, H. J. Zhao, Z.Y. Tang and D. Wang, *Angew. Chem. Int. Ed.*, 2013, **52**, 1–5.

11 D. W. Su, X. Q. Xie, P. Munroe, S. X. Dou and G. X. Wang, *Sci. Rep.*, 2014, **4**, 6519.

12 L. Chao, T. Q. Chen, W. J. Xu, X. B. Lou, L. K. Pan, Q. Chen and B. W. Hu, *J. Mater. Chem. A*, 2015, **3**, 5585–5591.

13 Y. Y. Chen, Y. Wang, H. X. Yang, H. Gan, X. W. Cai, X. M. Guo, B. Xu, M. F. Lü and A. H. Yuan, *Ceram. Int.*, 2017, **43**, 9945-9950.

14 L. Zhou, L. C. Yang, P. Yuan, J. Zou, Y. P. Wu and C. Z. Yu, *J. Phys. Chem. C*, 2010, **114**, 21868–21872.

15 Y. Zhao, N. Q. Zhang and K. N. Sun, *J. Mater. Chem. A*, 2013, **1**, 221–224.

16 M. H. Chen, J. L. Liu, D. L. Chao, J. Wang, J. H. Yin, J. Y. Lin, H. J. Fan and Z. X. Shen, *Nano Energy*, 2014, **9**, 364-372.

17 Y. Wang, X. M. Guo, Z. K. Wang, M. F. Lü, B. Wu, Y. Wang, C. Yan, A. H. Yuan and H. X. Yang, *J. Mater. Chem. A*, 2017, DOI: 10.1039/C7TA08314A.

18 M. C. Sun, M. F. Sun, H. X. Yang, W. H. Song, Y. Nie and S. N. Sun, *Ceram. Int.*, 2017, **43**, 363-367.

Journal of Materials Chemistry A Accepted Manuscript

19 S. Bhuvaneswari, P. M. Pratheeksha, S. Anandan, D. Rangappa, R. Gopalanb and Tata N. Raoa, *Phys. Chem. Chem. Phys.*, 2014, **16**, 5284–5294.

20 J. Liu, X. J. Xu, R. Z. Hu, L.C. Yang, and M. Zhu, *Adv. Energy Mater.*, 2016, **6**, 1600256.

21 Y. T. Zuo, G. Wang, J. Peng, G. Li, Y. Q. Ma, F. Yu, B. Dai, X. H. Guo and C. P. Wong, *J. Mater. Chem. A*, 2016, **4**, 2453-2460.

22 H. D. Liu, Z. L. Hu, H. B. Ruan, R. Hu, Y. Y. Su, L. Zhang and J. Zhang, *J Mater Sci: Mater Electron*, 2016, **27**, 11541-11547.

23 H. B. Wu, J. S. Chen, X. W. Lou and H. H. Hong, *J. Phys. Chem. C*, 2011, **115**, 24605-24610.

24 H.X. Yang and L. Li, *J. Alloys Compd.,* 2014, **584**, 76-80.

25 Y. J. Hong, M. Y. Son and Y. C. Kang, *Adv. Mater.* 2013, **25**, 2279-2283.

26 D. Z. Kong, J. S. Luo, Y. L. Wang, W. N. Ren, T. Yu, Y. S. Luo, Y. P. Yang and C. W. Cheng, *Adv. Funct. Mater*. 2014, **24**, 3815–3826.

27 Y. Zhao, X. Li, B. Yan, D. Xiong, D. Li, S. Lawes and X. L. Sun, *Adv. Energy Mater*, 2016, **6**, 1502175.

28 C. T. Cherian , J. Sundaramurthy , M. V. Reddy , P. Suresh Kumar , K. Mani , D. Pliszka , C. H. Sow , S. Ramakrishna and B. V. Chowdari, *ACS Appl. Mater. Interfaces*, 2013, **5**, 9957–9963 .

29 M. S. Wu and H. W. Chang, *J. Phys. Chem. C.*, 2013, **117**, 2590–2599.

30 X. H. Cao, C. L. Tan, M. Sindoro, and H. Zhang, *Chem. Soc. Rev.*, 2017, **46**, 2660–2677.

31 B. Y. Guan, X.Y. Yu, H. B. Wu and X. W. Lou, *Adv. Mater.*, 2017, **29**, 1703614.

32 Y. V. Kaneti, J. Tang, R. R. Salunkhe, X. C. Jiang, A. B. Yu, K. C. W. Wu, and Y. Yamauchi, *Adv. Mater.,* 2017, **29**, 1604898.

33 C. Z. Yuan, H. B. Wu, Y. Xie, and X. W. (David) Lou, *Angew. Chem. Int. Ed.*, 2014, **53**, 1488 – 1504.

34 L. Zhang, S. S. Zheng, L. Wang, H. Tang, H. G. Xue and G. X. Wang, *Small*, 2017, **13**, 1700917.

35 Y. Q. Fan, H. B. Shao, J. M. Wang, L. Liu, J. Q. Zhang and C. N. Cao, *Chem. Commun.*, 2011, **47**, 3469–3471.

36 L. Q. Mai, F. Yang, Y. L. Zhao, X. Xu, L. Xu and Y. Z. Luo, *Nat. Commun.*, 2011, **2**, 381.

37 H. Yu, C. Guan, X. H. Rui, B. Ouyang, B. Yadian, Y. Z. Huang, H. Zhang, H. E. Hoster, H. J.

Fan and Q.Y. Yan, *Nanoscale*, 2014, **6**, 10556–10561.

38 Y. N. Ko, Y. C. Kang and S. B. Park, *RSC Adv.*, 2014, **4**, 17873–17878.

39 X. Liu, Y. Lyu, Z. Zhang, H. Li, Y. Hu, Z. Wang, Y. Zhao, Q. Kuang, Y. Dong, Z. Liang, Q. Fan and L. Chen, *Nanoscale*, 2014, **6**, 13660–13660.

40 L. Q. Mai, F. Yang, Y. L. Zhao, X. Xu, L. Xu and Y. Z. Luo, *Nat. Commun*., 2011, **2**, 381.

41 K. S. Park, S. D. Seo, H. W. Shim and D. W. Kim, *Nanoscale Res. Lett.*, 2012, **7**, 35.

42 C. T. Cherian, M. V. Reddy, S. C. Haur and B. V. R. Chowdari, *ACS Appl. Mater. Interfaces*, 2013, **5**, 918–923.

43 Y. Yang, S. T. Wang, C. H. Jiang, Q. C. Lu, Z. L. Tang and X. Wang, *Chem. Mater*., 2016, **28**, 2417–2423.

44 Y. X. Wang, Y. Wu, L. L. Xing, Q. Wang and X. Y. Xue, *J. Alloys Compd.,* 2016, **689**, 655–661.

45 B. Wang, S. M. Li, X. Y. Wu, J. H. Liu, W. N. Tian and J. Chen, *New J. Chem.*, 2016, **40**, 2259–2267.

46 Y. S. Wang, Y. F. Sun, X. Zhang, Y. H. Wen and J. X. Guo, *RSC Adv.*, 2016, **6**, 51710–51715.

47 (a) L. Zhang, H. B. Wu, S. Madhavi, H. H. Hng and X. W. Lou, *J. Am. Chem. Soc.*, 2012, **134**, 17388–17391. (b) L. Zhang, H.B. Wu, R. Xu and X.W. Lou, *CrystEngComm*, 2013, **15**, 9332 – 9335.

48 L. Hu, N. Yan, Q.W. Chen, P. Zhang, H. Zhong, X.R. Zheng, Y. Li and X.Y. Hu, *Chem. Eur. J.*, 2012, **18**, 8971–8977.

49 Y. Yan, F. H. Du, X. P. Shen, Z. Y. Ji, H. Zhou and G. X. Zhu, *Dalton Trans*., 2014, **43**, 17544–17550.

50 X. Yang, Y. B. Tang, X. Huang, H. T. Xue, W. P. Kang, W. Y. Li, T. W. Ng and C. S. Lee, *J. Power source*, 2015, **284**, 109–114.

51 D.Q. Zhu, F.C. Zheng, S.H. Xu, Y.G. Zhang and Q.W. Chen, *Dalton Trans.*, 2015, **44**, 16946–16952.

52 Y. Y. Chen, R. Cai, Y. X. Yang, C. Liu, A. H. Yuan, H. X. Yang and X. P. Shen, *J. Alloys Compd.*, 2017, **698**, 469–475.

53 L. Hu, P. Zhang, H. Zhong, X. R. Zheng, N. Yan and Q. W. Chen, *Chem. Eur. J.*, 2012, **18**, 15049–15056.

54 H. Guo, T. T. Li, W. W. Chen, L. X. Liu, X. J. Yang, Y. P. Wang, Y. C. Guo, *Nanoscale*, 2014,

6, 15168–15174.

55 G. Huang, L. L. Zhang, F. F. Zhang and L. M. Wang, *Nanoscale*, 2014, **6**, 5509–5515.

56 L. Liu, Z. B. Hu, L. M. Sun, G. Gao and X. F. Liu, *RSC Adv.*, 2015, **5**, 36575–36581.

57 H. Yu, H. Fan, B. Yadian, H. Tan , W. Liu, H. H. Hng, Y. Huang and Q. Yan, *ACS Appl. Mater. Interfaces*, 2015, **7**, 26751–26757.

58 F. C. Zheng, D. Q. Zhu, X. H. Shi and Q. W. Chen, *J. Mater. Chem. A*, 2015, **3**, 2815–2824.

59 J. G. Leipoldt, L. D. C. Bok and P. J. Cilliers, *Z. Anorg. Allg. Chem.*, 1974, **409**, 343.

60 R. C. Young, *J. Am. Chem. Soc.*, 1932, **54**, 1402.

61 S. L. Ma, S. Ren, Y. Ma, D. Z. Liao and S. P. Yan, *Struct.Chem.*, 2009, **20**, 145.

62 M. Zhou, F. Lu, X. S. Shen, W. W. Xia, H. He and X. H. Zeng, *J. Mater. Chem. A*, 2015, **3**, 21201–21210.

63 L. J. Wang, X. H. Cui, L. L. Gong, Z.Y. Lyu, Y. Zhou, W. H. Dong, J. Liu, M. Lai, F. W. Huo, W. Huang, M. Lin and W. Chen, *Nanoscale*, 2017, **9**, 3898–3904

64 R. F. Nie, J. J. Shi, W. C. Du, W. S. Ning, Z. Y. Hou and F. S. Xiao, *J. Mater. Chem. A*, 2013, **1**, 9037–9045.

65 H. Li, L. Ming, W. W. Sun and Y. Wang, Adv. *Funct. Mater.*, 2016, **26**, 1098–1103.

66 M. Huang, K. Mi, J. H. Zhang, H. L. Liu, T. T. Yu, A. H. Yuan, Q. H. Kong and S. L. Xiong, *J. Mater. Chem. A*, 2017, **5**, 266–274.

67 C. H. Yan, G. Chen, X. Zhou, J. X. Sun and C. D. Lv, *Adv. Funct. Mater.,* 2016, **26**, 1428–1436.

68 J. Guo, H. Zhu, S. Zhou, Y. Sun and X. Zhang, *Ionics*, 2015, **21**, 2993–2999.

69 Y. Sun, J. Wang, B. Zhao, R. Cai, R. Ran and Z. Shao, *J. Mater.Chem. A*, 2013, **1**, 4736–4746.

70 Z. S. Wu, W. Ren, L. Wen, L. Gao, J. Zhao, Z. Chen, G. Zhou, F. Li and H. M. Cheng, *ACS Nano.*, 2010, **4**, 3187–3194.

71 Y. Xia, Z. Xiao, X. Dou, H. Huang, X. H. Lu, R. J. Yan, Y. P. Gan, W. J. Zhu, J. P. Tu, W. K. Zhang and X. Y. Tao, *ACS Nano*, 2013, **7**, 7083–7092.

72 Z. C. Yan, L. Liu, J. L. Tan, Q. Zhou, Z. F. Huang, D. D. Xia, H. B. Shu, X. K. Yang and X.Y. Wang, *J. Power Sources*, 2014, **269**, 37–45.

73 W. Y. Li, Z. P. Li, W. P. Kang, Y. B. Tang, Z. Y. Zhang, X. Yang, H. T. Xue, C.S. Lee and J. *Mater. Chem. A*, 2014, **2**, 12289–12295.

Journal of Materials Chemistry A Accepted Manuscript